5.3 An Up-to-1400nm 500MHz Demodulated Time-of-Flight Image Sensor on a Ge-on-Si Platform

C.-L. Chen*, S.-W. Chu*, B.-J. Chen*, Y.-F. Lyu*, K.-C. Hsu*, C.-F. Liang*, S.-S. Su, M.-J. Yang, C.-Y. Chen, S.-L. Cheng, H.-D. Liu, C.-T. Lin, K. P. Petrov, H.-W. Chen, K.-C. Chu, P.-C. Wu, P.-T. Huang, N. Na, S.-L. Chen

Artilux, Hsinchu, Taiwan, *Equally-Credited Authors (ECAs)

Indirect time-of-flight (iToF) image sensors on silicon platforms [1-3] are attracting rising attention because of their better immunity to background light and potential to achieve higher pixel resolution. Shifting the laser wavelength to 940nm [3] may further improve the outdoor performance but at a cost of reduced responsivity and lower modulation speed. As shown in red in Fig. 5.3.1, the solar irradiance at 940nm is only one-fourth of the case at 850nm, and it keeps going down with increasing wavelength and even vanishes at ~1350nm. To further increase the system SNR, using larger laser power is a feasible choice, but this introduces a laser safety issue [4]. The maximum permissible exposure (MPE) at the cornea versus laser wavelength with 0.1s exposure time is plotted in blue in Fig. 5.3.1 as well. Obviously, the exposure limit is quite stringent at 940nm, but much relaxed at a longer near-infrared (NIR) wavelength. Both curves in Fig. 5.3.1 indicate that a better SNR can be achieved with lasers emitting at a longer NIR wavelength, while the system can still satisfy the constraint of MPE. Unfortunately, traditional silicon solutions fail to operate at a wavelength beyond 1000nm because of the 1.1eV indirect bandgap. However, it is shown that this can be solved by using germanium-on-silicon (Ge-on-Si) as the absorption material [5]. Since Ge has a direct bandgap of 0.8eV, Ge-on-Si technology can extend the absorption wavelength up to nearly 1550nm.

In this work, we present an iToF image sensor on a Ge-on-Si platform to achieve improved absorption efficiency and higher modulation speed up to 1400nm wavelength. A block diagram of the demonstrated image sensor is shown in Fig. 5.3.2. In this prototype, a 240×180 image sensor array is implemented as a proof of concept. Four-phase system clocks are generated from a conventional Integer-N PLL for modulation and demodulation. Before sending to the pixel array and external illumination driver, these clocks are gated and conditioned by the timing generator for a preset integration time and different operation modes. A programmable delay line is added in the illumination driver path, which is explained below. A readout circuit bridges the image sensor array to column ADCs and the ADC outputs are further processed and integrated in the digital domain before reaching the output interface. The output interface is mainly composed of a 2-lane, 1.2Gb/s D-PHY MIPI transmitter. Additional CMOS outputs are also available for low-speed/low-cost systems. Two voltage domains are needed for this image sensor. The higher one (VDDH) receives a voltage >2.7V and the lower one (VDDL) receives a voltage of 1.8V. A temperature sensor is also implemented for the possible use of depth calibration and power control. All the blocks can be accessed through an I2C interface.

The iToF image sensor is developed in a back-side illumination (BSI) configuration, in which the Ge region is only available in the top wafer and the circuits are located in the bottom wafer to simplify the integration process. These 2 wafers are bonded together through a wafer bonding interface. A cross-section of the pixel region is shown in Fig. 5.3.3. The pixels follow a 2-tap lock-in pixel architecture [5]. The differential demodulation clocks (CLKP and CLKN) are distributed on the top wafer so as to create a continuously switching lateral electric field at the Ge surface (the side closer to VIA) between nodes Demod1 and Demod2 in every pixel. The photo-charges are collected through nodes FD1 and FD2. Since most of the photo-charges are generated inside the Ge layer and the Ge layer is very thin, the lateral electric field at the Ge surface can effectively sweep the photo-charges to node FD1 or FD2. Moreover, the transit time for the photo-charges drifting to node FD1 or FD2 is short, again, due to the thin Ge layer, and therefore the demodulation speed is significantly improved. To minimize the coupling to any sensitive high-impedance node and relax the design rule requirement, only FD1 and FD2 are interacted with the wafer bonding interface overlapping with the pixel area. The CLKP and CLKN are routed to the bottom-wafer clock drivers outside the pixel region. The pixel demodulation drivers are realized with tapered inverter chains and the supply of the inverter chains can be adjusted to maximize performance. The pixel circuits are implemented as a differential 4-transistor architecture. A simplified timing diagram is also shown in the bottom of Fig. 5.3.3. Before every exposure, all pixels are reset through Msh1/Msh2 and Mrt1/Mrt2. After optical exposure, integration, and demodulation, the collected photo-charges are stored on C1 and C2. Finally, the readout is accomplished through the source follower Msf1/Msf2 and the row-select switch Mbt1/Mbt2. A 4-quad measurements are implemented to recover the depth information without suffering from analog non-idealities.

All the demodulated pixel voltages are passed to the readout circuit and ADC before digital processing. As shown in Fig. 5.3.4, the readout circuit consists of sample-and-hold circuits and buffers. 2 signal paths are realized and can be activated in a time-interleaved way. Every pixel can be read out twice to reduce the circuit noise by 3dB. The ADC is designed with a SAR architecture and the output bit width is 9-12 depending on the system's operating scenario. The full-scale voltage (Vfs) of this ADC can be adjusted according to the input voltage swing, which results in lower quantization noise contribution. The programmable delay line and a pre-driver for external illumination driver are also depicted in the bottom of Fig. 5.3.4. The programmable delay line covers a range from 0° to 90° and more delays can be obtained by the quadrature post-divider inside the PLL. Assuming the modulation/demodulation waveforms are all square waves, the standard deviation of the recovered depth (σ_{depth}) shows a dependency on the initial phase offset, which is plotted in the bottom-left of Fig. 5.3.4. Under the same intensity of illumination, the σ_{depth} goes up and down with a period of 90°. This is because the noise transfer function changes with phase offset, assuming a fixed amount of collected photo-charges. Theoretically, choosing the optimized phase offset results in 1.4× improvement in SNR. For some applications where only relative depth is important, e.g., robotic arms and 3D scanning, an optimized phase offset can be introduced deliberately to maximize performance. If needed, the introduced offset can be calibrated at the module level.

This image sensor is developed via TSMC's 12-inch image sensor platform. Figure 5.3.5 shows a brief summary and comparison with recently published iToF image sensors. Because of the limited choice in commercial NIR camera lenses and bandpass filters, the image sensor module, including the NIR coating, are optimized at 940nm. All pixel parameters are measured by wafer-level probing. The external responsivity of the pixels is about 0.5A/W up to 1400nm, although the microlens is optimized at 940nm as well. The modulation frequency is between 10 and 500MHz, which is limited by the on-chip PLL. The demodulation contrast can be set between 0.7 and 0.9 by controlling the voltage of CLKP/CLKN. The standard deviations for indoor and outdoor scenarios are less than 0.5% and 0.55%, respectively. This image sensor consumes 200mW under typical operation. The depth images at 940nm wavelength are shown in Fig. 5.3.6. To create a consistent environment, we emulate the outdoor environment with a controlled high-power halogen lamp. The halogen lamp power is calibrated with NIR meter to make sure the optical power intensity at 940nm is equivalent to that from a ~100klux daylight. Thanks to the high absorption efficiency of Ge, we found very little difference between indoor and outdoor results. The die photo with labeled size is shown in Fig. 5.3.7. We believe the demonstrated iToF image sensor opens the possibility for operating at a longer NIR wavelength. The performance can be further improved by optimizing the microlens, bandpass filter, camera lens, and laser source at the desired wavelengths.

References:

[1] C. S. Bamji et al., "1Mpixel 65nm BSI 320MHz Demodulated TOF Image Sensor with 3.5um Global Shutter Pixels and Analog Binning," *ISSCC*, pp. 94-95, Feb. 2018.

[2] Y. Kato et al., "320x240 Back-Illuminated 10um CAPD Pixels for High Speed Modulation Time-of-Flight CMOS Image Sensor," *IEEE Symp. VLSI Circuits*, pp. C288-C289, June 2017.

[3] M.-S. Keel et al., "A 640x480 Indirect Time-of-Flight CMOS Image Sensor with 4-tap 7-um Global Shutter Pixel and Fixed-Pattern Phase Noise Self-Compensation Scheme," *IEEE Symp. VLSI Circuits*, pp. C258-C259, June 2019.

[4] IEC 60825-1 Ed. 2.0 (2007); Safety of laser products – Part 1: Equipment Classification and Requirements.

[5] N. Na et al., "High-Performance Germanium-on-Silicon Lock-in Pixels for Indirect Time-of-Flight Applications," *IEEE IEDM*, pp. 751-754, Dec. 2018.

 978-1-7281-3205-1/20/$31.00 ©2020 IEEE

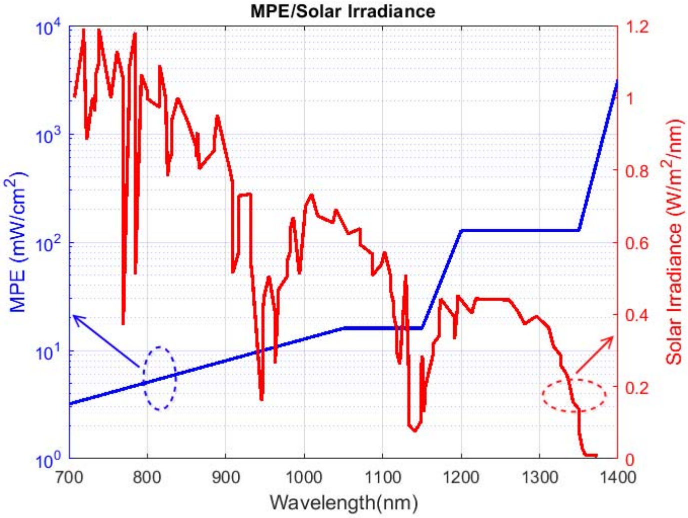

Figure 5.3.1: MPE/Solar Irradiance versus wavelength.

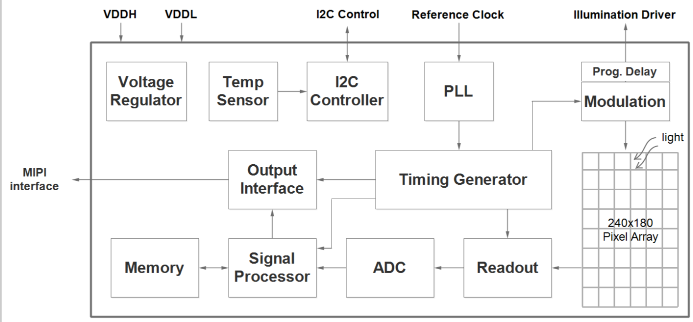

Figure 5.3.2: Block diagram of the iToF image sensor.

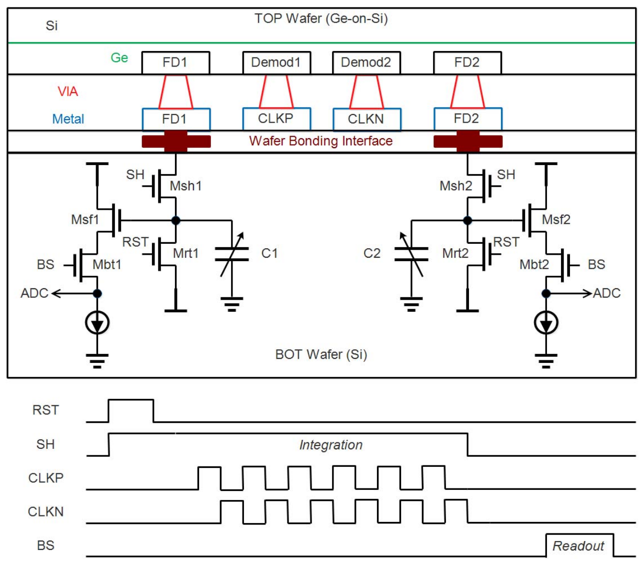

Figure 5.3.3: Architecture and operation principle of the pixel.

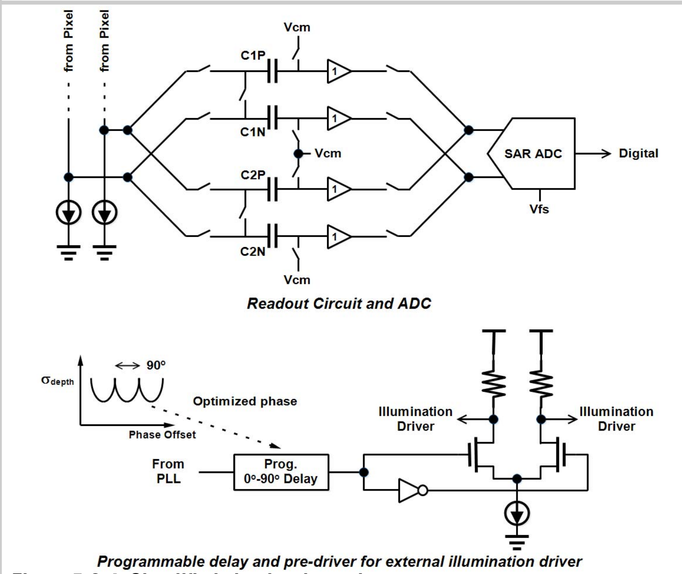

Figure 5.3.4: Simplified circuit schematics.

	ISSCC'18 [1]	VLSI'17[2]	VLSI'19[3]	This Work	
Pixel type	Si	Si	Si	Ge-on-Si	
Pixel pitch (um)	3.5	10	7	10	
Wavelength (nm)	860	850	940	850-1400	
Responsivity (A/W)	0.305	0.343	0.227	940nm	1310nm
				> 0.49*	> 0.54*
Resolution	1024x1024	320x240	640x480	240x180	
Modulation Frequency	10-320MHz	< 100MHz	10-150MHz	10-500MHz	
Demod. Contrast	0.87@200MHz	0.85@100MHz	0.86@100MHz	0.7-0.9 @ 500MHz depends on setting	
Std. @ 1m (%)	< 0.2	0.6	0.5	Indoor 940nm	Outdoor 940nm
				< 0.5	< 0.55

*: Post microlens, microlens efficiency optimized at 940nm

Figure 5.3.5: Summary and comparison table.

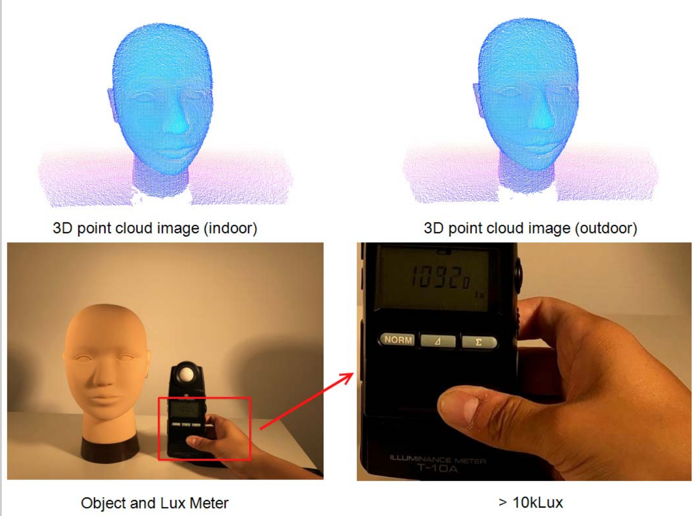

Figure 5.3.6: Depth images at 940nm.

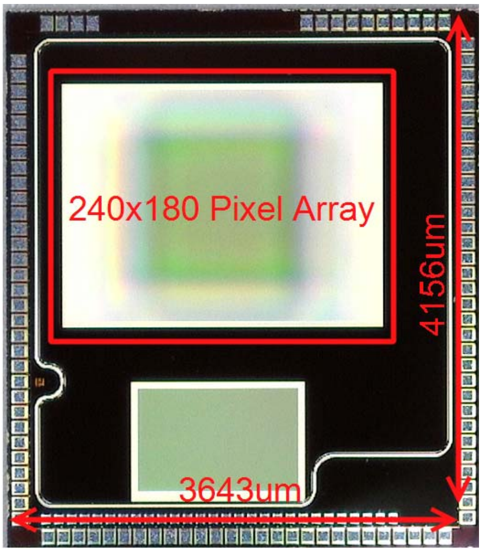

Figure 5.3.7: Die photo.

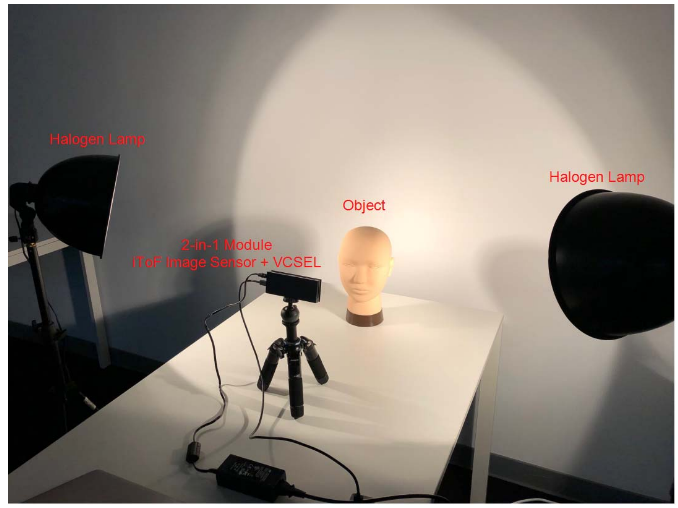

Figure 5.3.S1: Measurement setup for 3D images. The halogen lamp power is calibrated with an NIR meter to make sure the optical power intensity at 940nm is equivalent to that from a ~100klux daylight.

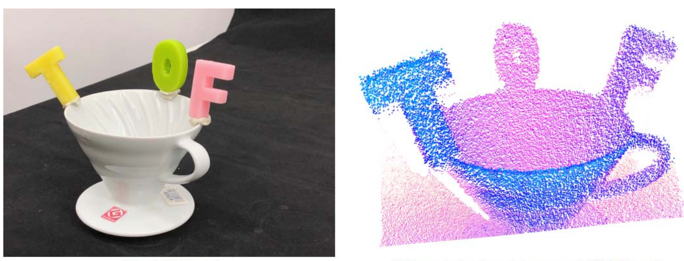

Figure 5.3.S2: Depth images at 1310nm. Because all the optical components are optimized at 940nm, the sensor receives little signal power and large ambient noise, which results in poor image quality.

Assuming demodulation contrast = 1, the standard deviation of depth σ_{depth} can be expressed as:

$$\sigma_{depth} \propto \frac{\sqrt{(N0^2+N90^2)\cdot(N_L+N_{AD}+N_{CKT}^2)}}{Fmod\cdot(N0+N90)^2}$$

Where N0 is the sum of the absolute photo-electrons in 0° and 180° measurement, N90 is the sum of the absolute photo-electrons in 90° and 270° measurement, N_L = N0+N90 = Constant, N_{AD} is the noise contributed by ambient light and dark current, and N_{CKT} is the noise of reset switches and ADC. For N0 > 0 and N90 > 0, it can be shown that:

$$N_L\cdot\frac{1}{\sqrt{2}} \leq \frac{\sqrt{(N0^2+N90^2)}}{(N0+N90)^2} \leq N_L$$

As a result, under the same modulation frequency, illumination power, and environment, changing the phase offset may affect σ_{depth} by a factor of 1.4.

Figure 5.3.S3: σ_{depth} dependency on phase offset. The phase offset can be adjusted in the pre-driver so as to achieve better image quality.

978-1-7281-3205-1/20/$31.00 ©2020 IEEE